DOI: 10.1002/ejic.200901119

A Facile Approach to Fabrication of Hexagonal-Phase $NaYF_4$:Yb^{3+}, Er^{3+} Hollow Nanospheres: Formation Mechanism and Upconversion Luminescence

Junwei Zhao,[a,b,c] Xiaomin Liu,[a] Di Cui,[d] Yajuan Sun,[a] Yi Yu,[a] Yifei Yang,[a] Chuang Du,[a] Yu Wang,[a,b,c] Kai Song,[a] Kai Liu,[a,b,c] Shaozhe Lu,[a] Xianggui Kong,*[a] and Hong Zhang*[c]

Keywords: Hydrothermal synthesis / Rare earths / Crystal growth / Polymers / Luminescence / Ostwald ripening

The hexagonal-phase $NaYF_4$:Yb^{3+}, Er^{3+} hollow nanospheres (HNS) have been successfully prepared for the first time by means of a hydrothermal route with the aid of polyethylenimine (PEI) as a surfactant. The nitrogen adsorption/desorption isotherms demonstrated the porous nature of the $NaYF_4$ HNS. The formation mechanism was explored based on the effects of the reaction parameters. The $NaYF_4$ solid spheres underwent a dissolution-recrystallisation transformation and a hollowing process when the hydrothermal reaction time was prolonged. The localised Ostwald ripening mechanism was proposed to account for the formation of $NaYF_4$ HNS, in which loose aggregations were found to be crucial. The upconversion luminescence of $NaYF_4$:Yb^{3+}, Er^{3+} HNS was also investigated. It is expected that these $NaYF_4$ HNS might have potential in applications as building blocks for biolabels and drug-delivery.

Introduction

Luminescence upconversion nanoparticles doped with rare earth ions have attracted much attention in recent years owing to their superior spectroscopic properties,[1] which may result in potential applications in many fields such as lasers, generation imaging devices and near-infrared quantum counting devices, especially in biology or biomedicine.[2] Among these materials, β-$NaYF_4$ has been reported as one of the most efficient hosts for performing infrared-to-visible photon conversion in the doped rare earth ions.[3,4] Up to now, various morphological $NaYF_4$ products have been synthesised by different synthetic methods.[5] However, few reports have focussed on the β-$NaYF_4$ hollow spheres which are much more desirable for biolabels and drug-delivery applications. Only very recently, α-$NaYF_4$ hollow nanospheres have been obtained by an ion exchange process.[6] It is known that the upconversion efficiency of β-$NaYF_4$ is significantly higher than the α-phase counterpart.[3,7] Hence, it is necessary to explore feasible and easily controllable synthetic approaches to obtain β-$NaYF_4$ hollow spheres with porous shells.

Significant progress has been made in the synthesis of hollow inorganic micro- and nanostructures.[8–16] Generally, preparation of the hollow inorganic micro- and nanostructures with template methods follows two effective approaches: (i) template-directed synthesis with hard templates[17–19] such as polymer latex particles, silica spheres, and metal nanoparticles, and (ii) soft templates[20–23] such as emulsion droplets, micelles, and gas bubbles. However, the resultant hollow structures usually suffer from some weaknesses, e.g. high cost and tedious synthetic procedures and these factors may limit their applications.[24] Ideally, one would like to explore a one-step template-free method for controllable synthesis of hollow structures. Most recently, a number of template-free methods for generating hollow inorganic micro- and nanostructures has been developed based on novel mechanisms,[25–30] including the nanoscale Kirkendall effect or Ostwald ripening.

In this paper, we report the one-step hydrothermal synthesis of β-$NaYF_4$ HNS with mesopores on the shells, using PEI as a surfactant. The formation of the products undergoes an Ostwald ripening mechanism from α-$NaYF_4$ solid submicron-spheres to β-$NaYF_4$ HNS, which was apparent by investigating the effects of reaction conditions on the morphologies and sizes of the $NaYF_4$ products, such as the concentration of the aqueous PEI solution and the hydrothermal reaction temperature and time. This method can provide a high-yield mass production of inorganic hollow structures in aqueous solution at relatively low temperatures. The absorptive capacity and upconversion lumines-

[a] Key Laboratory of Excited-State Processes, Changchun Institute of Optics, Fine Mechanics and Physics, Chinese Academy of Sciences,
Changchun 130033, P. R. China
E-mail: xgkong14@ciomp.ac.cn
[b] Graduate School of Chinese Academy of Sciences,
Beijing 100039, P. R. China
[c] Van't Hoff Institute for Molecular Sciences, University of Amsterdam,
Nieuwe Achtergracht 166, 1018 WV Amsterdam, The Netherlands
E-mail: h.zhang@uva.nl
[d] College of Chemistry, University of Wuhan,
Wuhan 430072, P. R. China

cence of the final products were also investigated. The prepared β-$NaYF_4$:Yb^{3+}, Er^{3+} HNS can be dispersed in aqueous media due to the presence of the PEI polymer. The spheres may act as promising drug-delivery carriers and fluorescence labelling materials owing to their hollow interior structures and superior luminescence upconversion spectroscopic properties.

Results and Discussion

Structure and Morphology

The synthetic conditions and characteristics of samples prepared by the hydrothermal route are listed in Table 1 and the optimal synthetic parameters for HNS are given, i.e. a PEI concentration of approximately 5 wt.-% and a hydrothermal time of 24 h at a temperature of 160 °C. The pH values were kept at 8–9 in all cases for the purpose of exploring the influence of other parameters. It was found that the PEI concentration, the hydrothermal temperature and time were the key factors for the crystal structure, size and/or morphology of the samples and this will be discussed later.

Figure 1 shows the X-ray powder diffraction (XRD) pattern of the prepared product obtained with a 5 wt.-% concentration of the aqueous PEI solution under hydrothermal treatment at 160 °C for 24 h (sample 7 in Table 1). The XRD pattern of the material confirms its hexagonal crystalline nature and most of the strong peaks match well with those of standard β-$NaYF_4$ (PDF card No. 160334).

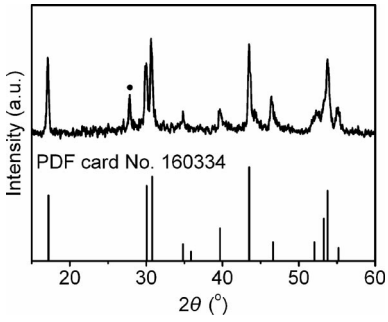

Figure 1. XRD pattern of the $NaYF_4$:Yb^{3+}, Er^{3+} phosphors prepared by hydrothermal treatment at 160 °C for 24 h with a 5 wt.-% concentration of the aqueous PEI solution. The black dot (•) represents the peak (28.42) of the α phase.

Only one impurity peak can be distinguished in the XRD pattern and this may come from α-$NaYF_4$ (PDF card No. 060342). The peaks shown in the XRD pattern are sharp and intense, indicating good crystallisation of the sample.

The scanning electron microscopy (SEM) and transmission electron microscopy (TEM) images with different magnifications and the energy-dispersive X-ray spectrometer (EDS) spectrum of the $NaYF_4$:Yb^{3+}, Er^{3+} product are shown in Figure 2. From Figure 2 (a, b) it can be seen that the product consists of uniform spheres of about 500 nm in size, themselves composed of many smaller particles of about 50 nm. The broken spheres are hemispherical or bowl-like shaped, indicating that the spheres have a hollow structure (Figure 2, see part c and the inset). The EDS result determined the chemical compositions of the products as shown in Figure 2 (d) and this demonstrates that the samples contain Na, Y, Yb, Er and F, from which the exis-

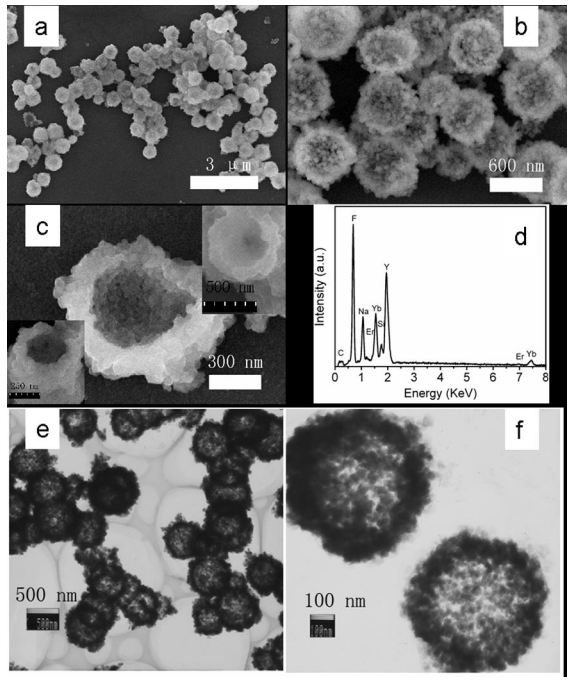

Figure 2. SEM and TEM images with different magnifications (a, b, c, e, f) and the EDS (d) spectrum of $NaYF_4$:Yb^{3+}, Er^{3+} HNS prepared under hydrothermal treatment at 160 °C for 24 h with a 5 wt.-% concentration of the aqueous PEI solution. Inset: SEM images of the broken spheres.

Table 1. Synthetic conditions and characteristics of the samples prepared by means of the hydrothermal method.

Sample	PEI concentration	Hydrothermal temperature / °C	Hydrothermal time / h	Phase	Morphology	Reference
1	5 wt.-%	120	24	α and β	flower-like	Figure 5, c
2	5 wt.-%	200	24	α and β	flower-like and bulk	Figure 5, d
3	5 wt.-%	160	0	amorphous	aggregate	Figure 6, a
4	5 wt.-%	160	0.5	α	spheres	Figure 6, b
5	5 wt.-%	160	1	α and β	spheres and flosses	Figure 6, c
6	5 wt.-%	160	1.5	α and β	spheres and flosses	Figure 6, d
7	5 wt.-%	160	24	β	hollow spheres	Figure 2
8	10 wt.-%	160	24	α	spheres	Figure 5, b
9	2 wt.-%	160	24	α and β	flower-like and bulk	Figure 5, a

tence of sodium yttrium fluoride can be inferred. The weak C peak should probably be attributed to CO_2 adsorbed by the sample and the weak Si peak originates from the silicon support. To further confirm the hollow nature of the $NaYF_4$ spheres, TEM studies were carried out and the results are exemplified in Figure 2 (e, f). A strong contrast between the dark edges and the pale centre in the bright field TEM images verified that the $NaYF_4$ spheres have a hollow interior (Figure 2, e). The thickness of the $NaYF_4$ HNS are around 120 nm (Figure 2, f). Template synthesis is a known general approach for obtaining hollow spheres whereby the template serves as a scaffold against which other materials are assembled with a morphology similar to that of the template. In this work, however, the monodispersive $NaYF_4$ HNS were synthesised without additional other templates and in aqueous solution using PEI as a surfactant.

To investigate the specific surface area and porous nature of the $NaYF_4$ HNS, the Brunauer–Emmett–Teller (BET) gas-sorption measurement was carried out. The recorded N_2 adsorption-desorption isotherms for the product show significant hysteresis at relative pressures P/P_0 above 0.75 (Figure 3). The sample exhibits classic type IV behaviour for mesoporous structures or type II behaviour for macroporous structures.[31] The observed hysteresis loops shift to a high relative pressure $P/P_0 \approx 1$, suggesting the presence of large pores (> 50 nm).[32,33] The BET surface area of the sample is about 13.4 $m^2 g^{-1}$ calculated from N_2 isotherms at 77 K. The pore size distribution of $NaYF_4$ HNS (see inset in Figure 3) indicates pore-size distributions in the mesoporous (2–50 nm) and macroporous (> 50 nm) regions with a maximum peak pore diameter of ca. 128 nm. According to previous reports,[32,33] these mesopores and macropores presumably arise from the interstices among the $NaYF_4$ nanoparticles within the shells and the central hollows of $NaYF_4$ HNS, respectively.

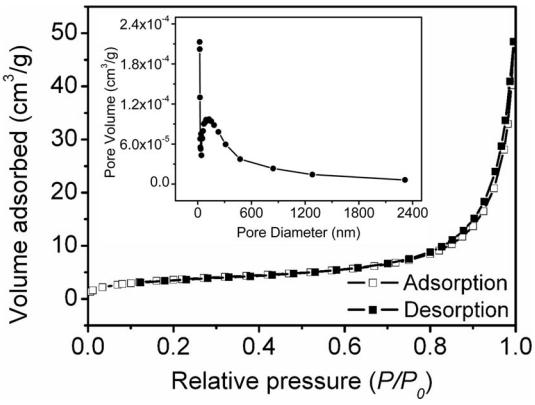

Figure 3. Nitrogen adsorption-desorption isotherms of the $NaYF_4$:Yb^{3+}, Er^{3+} HNS. Inset shows the pore size distribution obtained from the adsorption curve.

To demonstrate the existence of PEI polymer adsorbed on the surface of the nanoparticles, the Fourier transform infrared (FTIR) spectrum of the $NaYF_4$:Yb^{3+}, Er^{3+} HNS was recorded as shown in Figure 4. The absorption bands around 3308 cm^{-1} for the sample correspond to the OH stretching vibrations[34] originating from the absorption of H_2O. The weak bands at ca. 2928 and 2856 cm^{-1} are, respectively, the asymmetric and symmetric stretching vibration modes of the CH_2 group.[35] Peaks at ca. 1633 and 1429 cm^{-1} are related to the vibrations of the amide bonds and CH_2 group of the PEI polymer, respectively.[35]

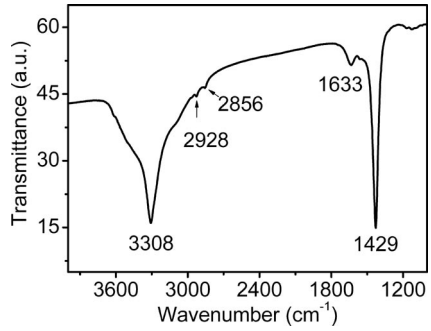

Figure 4. FTIR spectra of the $NaYF_4$:Yb^{3+}, Er^{3+} HNS.

To comprehend the formation mechanism of the $NaYF_4$:Yb^{3+}, Er^{3+} HNS, controlled experiments were performed. The SEM images of the products prepared under different PEI concentrations are shown in parts a and b of Figure 5. The PEI concentration was taken as 2, 5 or 10 wt.-%. In general, a relatively high PEI concentration did not favour the formation of hollow spheres but formation of solid spheres with smooth surfaces. For example, when the concentration of PEI was 10 wt.-% in the solution, the $NaYF_4$ smooth spheres were obtained as the predominant products (Figure 5, a). The TEM image confirmed the solid character of the sample (see inset in Figure 5, a). With a decrease in the concentration of PEI, the quantity of $NaYF_4$ HNS increased markedly. When the PEI concentration decreased to 5 wt.-%, a high yield of $NaYF_4$ HNS was obtained (see Figure 2). When the PEI concentration was decreased to 2 wt.-% or even lower, the products included, in addition to hollow spheres, solid spheres and predominantly bulk prism-like materials (Figure 5, b). It can thus be concluded that an appropriate PEI concentration (e.g., 5 wt.-%) is indispensable for the formation of $NaYF_4$ HNS. The effect of the hydrothermal temperature on the morphology of the product was also evaluated. A series of $NaYF_4$ samples was prepared from the precursor suspensions through hydrothermal treatment at 120, 160 and 200 °C for 24 h, while the rest of the experimental parameters and conditions remained the same. The SEM images of the products are shown in Figure 5 (c, d). The dominant product consisted of flower-like microstructures with a diameter of about 1 μm when the hydrothermal temperature was 120 °C (Figure 5, c). From the magnified image shown in the inset of Figure 5 (c), the microstructures are clearly constructed from lots of nanoplates which exhibit a tendency to assemble into large hollow particles. When the hydrothermal temperature increased to 160 °C, a high yield of $NaYF_4$ HNS was obtained (see Figure 2). Further increas-

ing the hydrothermal temperature to 200 °C or even higher, resulted in the sizes of the flower-like microstructures being nearly the same but most of them became incompact and the bulk prism-like materials appeared in greater abundance (Figure 5, d).

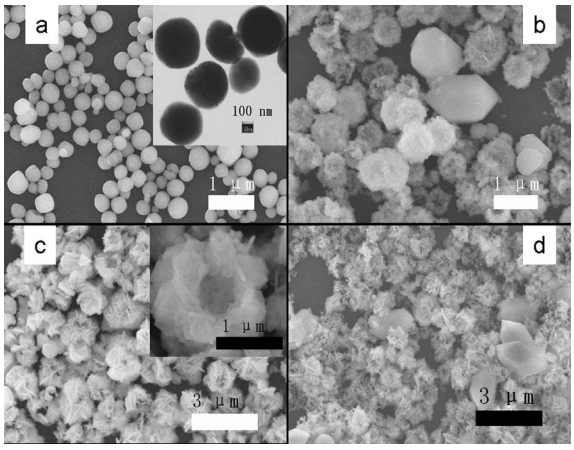

Figure 5. SEM images of $NaYF_4$:Yb^{3+}, Er^{3+} products prepared under different hydrothermal conditions: (a) 10 wt.-% PEI, (b) 2 wt.-% PEI (temperature: 160 °C, time: 24 h); (c) 120 °C, (d) 200 °C (PEI concentration: 5 wt.-%, time: 24 h). Inset: TEM and magnified SEM images.

The SEM and TEM images and XRD patterns of the products prepared by isolating intermediate products at reaction stages of 0, 0.5, 1 and 1.5 h are shown in Figure 6. The precursor without hydrothermal treatment appeared as spherical aggregates with coarse surfaces (Figure 6, a). The corresponding XRD patterns indicated an amorphous structure [Figure 6, e (i)]. The $NaYF_4$ solid submicron-spheres were solely obtained when the reaction was carried out for 0.5 h (Figure 6, b). The XRD patterns of the sample matched well with α-$NaYF_4$ [Figure 6, e (ii)]. Further increasing the hydrothermal time to 1 h resulted in products composed of nanoparticles with smooth surfaces and the flocky spheres with coarse surfaces (Figure 6, c). Interestingly, the flocky spheres featured a core-shell structure – the core consists of solid spheres while the shell is an incompact layer of dandelion-like nanoflosses generated on the surfaces of submicron-spheres without visible gaps (inset in Figure 6, c) and the XRD patterns exhibited the mixed crystal structures of cubic and hexagonal phases [Figure 6, e (iii)]. It has been confirmed that the solid spheres were in the cubic phase. Therefore, it is reasonable to speculate that the dandelion-like nanoflosses were in the hexagonal phase. From these SEM images, it is apparent that the ratio of flocky spheres to solid particles increases with an increase in the hydrothermal reaction time. When the hydrothermal time was increased to 1.5 h, the core-shell structure became a core-void-shell structure and the interspaces between core and shell also became larger. Surprisingly, the increasing interspaces are the result of the decreasing size of the solid core rather than the swelling of the shell. Some of the solid spheres in the core position disappeared almost completely, implying that the solid spheres dissolved slowly as the hydrothermal time increased (Figure 6, d). In the meantime, the hexagonal phase became more apparent [Figure 6, e (iv)]. After hydrothermal treatment for 24 h, the $NaYF_4$ solid core was nearly completely consumed due to the outward mass transport to form the $NaYF_4$ shell, resulting in spherical void spaces in the centre of the submicron-spheres and β-$NaYF_4$ HNS were obtained (see Figure 2). The one impurity peak may come from α-$NaYF_4$ solid cores which were not consumed completely by some or other HNS (see Figure 1). These results indicate that the $NaYF_4$ solid microspheres underwent a dissolution-recrystallisation transformation and a hollowing process when the reaction time was prolonged and the β-$NaYF_4$ HNS are thermodynamically more stable structures than α-$NaYF_4$ solid spheres.[5f]

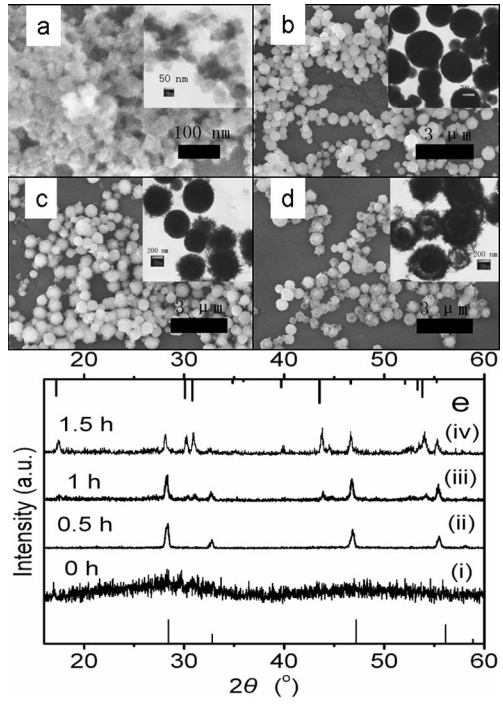

Figure 6. SEM and TEM (inset) images and XRD patterns of the products prepared by isolating intermediate products at different reaction stages: (a, i) 0 h (precursor); (b, ii) 0.5 h; (c, iii) 1 h; (d, iv) 1.5 h (temperature: 160 °C, PEI concentration: 5 wt.-%).

Possible Formation Mechanism of the HNS

The above results can be explained by assuming that a PEI-induced Ostwald ripening process is responsible for the formation of $NaYF_4$ HNS. The Ostwald ripening model was first proposed to explain the formation of TiO_2 HNS,[27] something which was further demonstrated in the formation of Cu_2O and ZnS HNS.[36] The possible formation mechanism of $NaYF_4$ HNS is shown by the schematic diagram in Scheme 1. At the beginning, a Ln-PEI complex colloid solution is mixed with NH_4F and NaCl solutions to rapidly produce a $NaLnF_4$ precursor at room temperature (step 1 in Scheme 1) and this can be proved by the light white suspension produced quickly by the reaction mixture.

Several recent reports have indicated that the existence of an appropriate amount of surfactant can modulate the kinetics of the crystal growth and determine the subsequent morphology of the products.[37] In our case, PEI may provide a favourable chemical environmental condition for the formation of α-$NaYF_4$ solid submicron-spheres during the hydrothermal process, which leads to the following hollow evolution process. For the current hydrothermal synthetic system, α-$NaYF_4$ solid submicron-spheres can be prepared at the very beginning due to the coordination effect of PEI (step 2 in Scheme 1). Some of the newly formed smaller α-$NaYF_4$ solid nanospheres exhibit higher surface energy due to their larger curvatures. As the hydrothermal process evolves, the energy provided by the reaction system becomes higher until a certain moment when it is high enough to overcome the reaction energy barrier. The α-$NaYF_4$ solid nanospheres become dissolved through a dissolution-recrystallisation process and the β-$NaYF_4$ dandelion-like nanoflosses are formed which are adsorbed on the larger α-$NaYF_4$ solid spheres (step 3 in Scheme 1) because the hexagonal phase is a thermodynamically more stable structure.[5f] As the hydrothermal time is prolonged and more monomers are consumed, the α-$NaYF_4$ solid crystals located in the inner cores will have a higher solubility due to the higher surface energies associated with their larger curvatures. Previous studies have demonstrated that Ostwald ripening will happen during this time because smaller, less well crystallised or less dense particles in a colloidal aggregate will be dissolved gradually, while larger, better crystallised or denser particles in the same aggregate are growing.[11,27] Therefore, the outer crystallites packed loosely of solid β-$NaYF_4$ nanowires would serve as starting growth sites for the subsequent recrystallisation. As the mass is transported, the void spaces in the microspheres are generated mainly through the Ostwald ripening (step 4 in Scheme 1). During this ripening process, the inner crystallites, which have a higher surface energy, will dissolve and transfer outside,[11,27,36b] producing channels connecting inner space and outer space in the β-$NaYF_4$ shells. This phenomenon could be observed in SEM and TEM images shown in Figure 6, where the density of the shells becomes looser with an increase in reaction time. The α-$NaYF_4$ cores could further be excavated with enough ripening time owing to the higher surface energy and $NaYF_4$ HNS with larger interiors are formed (step 5, 6 in Scheme 1).

It is generally accepted that the crystal growth habit is not only determined by the internal structure but is also affected by the external conditions.[38] Our experiment results reveal that the concentration of the aqueous PEI solution and the hydrothermal reaction temperature are the other two major factors affecting the morphologies and sizes of samples. The use of organic surfactants or polymers in solutions is a powerful approach for the synthesis of nano/microstructures with complex shapes and sizes. PEI is known to be one of the most powerful surfactants for the synthesis of nanostructures.[5e,39] In our case, when PEI is added into the reaction system, the strong Ln-PEI complex may be formed. The additive organic molecules in solution

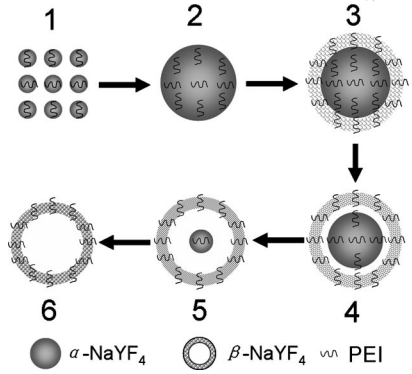

Scheme 1. Schematic illustration of a possible PEI-induced Ostwald ripening process for the formation of $NaYF_4$ HNS.

can affect the morphology of inorganic crystals by lowering the activation energy of nucleation of specific crystal faces and polymorphs through interfacial recognition if there is molecular complementarity at the crystal-additive interface.[40] We speculate that PEI molecules may bind to the crystal surfaces of the nanocrystals, which lowers the surface free energies of the crystallographic planes. The more PEI molecules that are added, the less the surface free energies of the reaction system. In this way, the thermodynamic equilibrium state is conserved during the growth stage of the nanocrystals and the nanoparticles are obtained when relatively higher concentrations of PEI solution are added into the reaction system (e.g., 10 wt.-%) and, thus, the dissolution-recrystallisation transformation cannot occur. When small amounts of PEI are added, the thermodynamic colloid could be unstable and the nanoparticles spontaneously grow by an Ostwald ripening process to reach a new thermodynamic equilibrium in which the β-$NaYF_4$ hollow structure is thermodynamically more stable than the α-$NaYF_4$ solid spheres, henceforth making the phase and morphology transformations occur. Similar to the concentration of aqueous PEI solution, the hydrothermal temperature also affects the balance of the thermodynamics and kinetics of the reaction system. Therefore, an optimal concentration of the aqueous PEI solution and an appropriate hydrothermal reaction temperature will provide a favourable chemical environment for the formation of $NaYF_4$ HNS.

Upconversion Luminescence Properties of $NaYF_4$: 20 mol-% Yb^{3+}, 2 mol-% Er^{3+} HNS

Upconversion luminescence processes of rare earth ions doped in solid materials have been widely investigated.[1] Figure 7 shows the upconversion luminescence spectra of the $NaYF_4$:20 mol-% Yb^{3+}, 2 mol-% Er^{3+} HNS upon irradiation with a CW diode laser at 980 nm. The green and red colour emissions observed in the range of 510–590 nm and 640–690 nm come from the 4f–4f electronic transitions ($^2H_{11/2}$, $^4S_{3/2}$)→$^4I_{15/2}$ and $^4F_{9/2}$→$^4I_{15/2}$ of the Er^{3+} ions. The inset in Figure 7 is the excitation power dependence of the upconversion spectra of the $NaYF_4$:20 mol-% Yb^{3+}, 2 mol-

% Er^{3+} HNS, where an increase in the emission intensity vs. the excitation power density is shown. It is well-known that $I_{em} \propto I_{exc}^{n}$ exists in upconversion processes. Fitting the data points yielded slopes of approximately 1.4 and 2.1 for the ($^2H_{11/2}$, $^4S_{3/2}$)→$^4I_{15/2}$ and $^4F_{9/2}$→$^4I_{15/2}$ transitions, respectively, indicating that the upconversion luminescence involves a two-photon absorption process. The fact that n is larger for the red emission indicates a faster population growth of the up-level involved in the red emission. In the upconversion nanomaterials, the dominant red emission indicates a large population of the $^4F_{9/2}$ level and a small population of the ($^2H_{11/2}$, $^4S_{3/2}$) levels. In our case, a relevant multiphonon relaxation process, which is regarded as one of the reasons for a strong red emission, is efficient due to the presence of the organic groups of high-vibrational frequency on the surfaces of the nanoparticles (see IR spectra in Figure 4).[5f] Similar phenomena were also observed in Lu_2O_3:Yb^{3+}, Er^{3+} nanocrystals.[41] Considering the relatively high concentration of Er^{3+} (2 mol-%), cross relaxation between two nearby Er^{3+} ions should occur and this may be another reason for the strong red emission and the high n.[42] Besides, the energy transfer between Er and Yb also plays an important role in the upconversion mechanism. However, a detailed analysis of the upconversion mechanism is not the focus of this paper − the authors leave such a discussion for a future work.

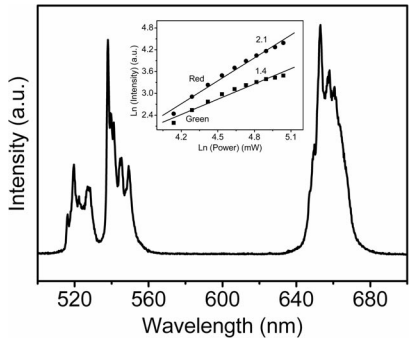

Figure 7. Upconversion luminescence spectra of $NaYF_4$:20 mol-% Yb^{3+}, 2 mol-% Er^{3+} HNS upon irradiation at 980 nm (power: 62 mW). Inset: pump power dependence of the upconverted green and red integrated intensities.

Conclusions

In summary, we have developed a one-step simple hydrothermal route for large-scale synthesis of β-$NaYF_4$ HNS. The obtained β-$NaYF_4$ HNS have excellent porous properties. The pore size distribution is in the mesoporous (2–50 nm) and macroporous (> 50 nm) regions. It has been confirmed that the hydrothermal time, hydrothermal temperature and PEI concentration play important roles in the growth process of the final product. The formation mechanism is related to the Ostwald ripening mechanism, in which the loose nanoflosses are the crucial step in the formation of $NaYF_4$ HNS. The obtained β-$NaYF_4$:20 mol-% Yb^{3+}, 2 mol-% Er^{3+} HNS demonstrate superior upconversion luminescence and can be dispersed in aqueous media due to the presence of PEI polymer, which may potentially act as promising drug-delivery carriers and fluorescence labeling materials.

Experimental Section

Materials: All reagents were analytical grade. $Ln(NO_3)_3{\cdot}6H_2O$ (lanthanide ion/Ln: Y, Yb, or Er) was freshly prepared by the reaction of Ln_2O_3 with nitric acid. Water was distilled and deionised using a Millipore Milli-Q Purication System, which has a resistivity not less than 18.2 MΩ PEI solution was purchased from Sigma–Aldrich (Product No. 408700).

Synthesis of $NaYF_4$:Yb^{3+}, Er^{3+} Samples: In a typical procedure for the preparation of $NaYF_4$: 20 mol-% Yb^{3+}, 2 mol-% Er^{3+} phosphors, an aqueous solution of $Ln(NO_3)_3{\cdot}6H_2O$ (0.2 mol L^{-1}, 5 mL, Y/Yb/Er = 78:20:2) was mixed with the 2–10 wt.-% concentration of the aqueous PEI solution (25 mL) with vigorous stirring leading to white precipitates of the lanthanide–PEI complex. A mixed aqueous solution of NaCl (0.2 mol L^{-1}, 5 mL) and NH_4F (1.2 mol L^{-1}, 10 mL) was then added slowly to the above complex and the pH value was adjusted to 8–9 with dilute hydrochloric acid. After stirring for 1 h, the resultant precursor solution was transferred to an autoclave. The autoclave was then placed in a digital temperature-controlled oven and heated at 120–200 °C for several hours and then cooled to room temperature naturally. Subsequently, the precipitate of $NaYF_4$:Yb^{3+}, Er^{3+} phosphors in the autoclave could be separated from the reaction media by centrifugation (6500 rpm, 15 min) and they were then filtered and washed several times with deionised water. After drying in a vacuum at 60 °C for 24 h, $NaYF_4$:Yb^{3+}, Er^{3+} phosphor was obtained. In the investigation of the synthetic mechanism, only one reaction parameter, i.e. the hydrothermal reaction time, temperature or PEI amount, was changed at a time while the remaining experimental parameters were kept the same.

Characterisation: The structures and morphologies of $NaYF_4$:Yb^{3+}, Er^{3+} phosphors were characterised using X-ray powder diffraction (XRD, Bruker D8-advance, Cu-K_α, λ = 1.5418 Å), scanning electron microscopy (SEM, Hitachi, S-4800) with an energy-dispersive X-ray spectrometer (EDS), transmission electron microscopy (TEM, FEI Tecnai G2 S-Twin) and Fourier transform infrared (FTIR) spectroscopy. The Brunauer–Emmett–Teller (BET) surface areas of the powders were measured by nitrogen adsorption using a Micromeritics ASAP 2020 nitrogen adsorption apparatus (USA). All the samples were degassed at 180 °C prior to nitrogen adsorption measurements. The BET surface area was determined by a multipoint BET method using the adsorption data in the relative pressure (P/P_0) range of 0.05–0.3. The desorption isotherm was used to determine the pore size distribution by the Barret–Joyner−Halender (BJH) method, assuming a cylindrical pore model.[31a] The nitrogen adsorption volume at a relative pressure (P/P_0) of 0.995 was used to determine the pore volume and average pore size. FTIR spectra were recorded with a Perkin–Elmer 580B infrared spectrophotometer with the KBr pellet technique. The upconversion emission spectra of $NaYF_4$:Yb^{3+}, Er^{3+} phosphors were acquired using a Jobin–Yvon LabRam Raman spectrometer system and a Peltier air-cooled CCD detector. The samples were excited by a continuous wavelength (CW) semiconductor diode laser at 980 nm. The maximal excitation power used in the experiment was about 154 mW with a focusing area of about 0.03 mm^2.

Acknowledgments

This work was financially supported by the exchange program between the Academy of Sciences of China and the Royal Netherlands Academy of Sciences of the Netherlands, and the National Natural Science Foundation of China (Grant No. 10904142 and 10874180).

[1] a) F. Auzel, *Chem. Rev.* **2004**, *104*, 139–173; b) M. Pollnau, D. R. Gamelin, S. R. Lüthi, H. U. Güdel, M. P. Hehlen, *Phys. Rev. B* **2001**, *61*, 3337–3346; c) P. S. Golding, S. D. Jackson, T. A. King, M. Pollnau, *Phys. Rev. B* **2000**, *62*, 856–864.

[2] a) F. van de Rijke, H. Zijlmans, S. Li, T. Vail, A. K. Raap, R. S. Niedbala, H. J. Tanke, *Nat. Biotechnol.* **2001**, *19*, 273–276; b) S. F. Lim, R. Riehn, W. S. Ryu, N. Khanarian, C. K. Tung, D. Tank, R. H. Austin, *Nano Lett.* **2006**, *6*, 169–174; c) L. Q. Xiong, Z. G. Chen, Q. W. Tian, T. Y. Cao, C. J. Xu, F. Y. Li, *Anal. Chem.* **2009**, *81*, 8687–8694.

[3] K. W. Krämer, D. Biner, G. Frei, H. U. Güdel, M. P. Hehlen, S. R. Lüthi, *Chem. Mater.* **2004**, *16*, 1244–1251.

[4] N. Menyuk, K. Dwight, J. W. Pierce, *Appl. Phys. Lett.* **1972**, *21*, 159–161.

[5] a) G. S. Yi, H. C. Lu, S. Y. Zhao, Y. Ge, W. J. Yang, D. P. Chen, L. H. Guo, *Nano Lett.* **2004**, *4*, 2191–2196; b) H. Schäfer, P. Ptacek, K. Kömpe, M. Haase, *Chem. Mater.* **2007**, *19*, 1396–1400; c) L. Y. Wang, Y. D. Li, *Chem. Mater.* **2007**, *19*, 727–734; d) G. S. Yi, G. M. Chow, *Adv. Funct. Mater.* **2006**, *16*, 2324–2329; e) F. Wang, D. K. Chatterjee, Z. Q. Li, Y. Zhang, X. P. Fan, M. Q. Wang, *Nanotechnology* **2006**, *17*, 5786–5791; f) J. W. Zhao, Y. J. Sun, X. G. Kong, L. J. Tian, Y. Wang, L. P. Tu, J. L. Zhao, H. Zhang, *J. Phys. Chem. B* **2008**, *112*, 15666–15672.

[6] F. Zhang, Y. F. Shi, X. H. Sun, D. Y. Zhao, G. D. Stucky, *Chem. Mater.* **2009**, *21*, 5237–5243.

[7] S. Heer, K. Kömpe, H. Güdel, M. Haase, *Adv. Mater.* **2004**, *16*, 2102–2105.

[8] X. W. Lou, Y. Wang, C. Yuan, J. Y. Lee, L. A. Archer, *Adv. Mater.* **2006**, *18*, 2325–2329.

[9] a) J. Geng, B. Liu, L. Xu, F. N. Hu, J. J. Zhu, *Langmuir* **2007**, *23*, 10286–10293; b) I. D. Hosein, C. M. Liddell, *Langmuir* **2007**, *23*, 2892–2897.

[10] X. M. Yin, C. C. Li, M. Zhang, Q. Y. Hao, S. Liu, Q. H. Li, L. B. Chen, T. H. Wang, *Nanotechnology* **2009**, *20*, 455503.

[11] a) J. Li, H. C. Zeng, *J. Am. Chem. Soc.* **2007**, *129*, 15839–15847; b) Z. Yang, Z. Niu, Y. Lu, Z. Hu, C. C. Han, *Angew. Chem. Int. Ed.* **2003**, *42*, 1943–1945.

[12] J. X. Wang, X. W. Sun, Y. Yang, C. M. L. Wu, *Nanotechnology* **2009**, *20*, 465501.

[13] D. Yu, X. Sun, J. Zou, Z. Wang, F. Wang, K. Tang, *J. Phys. Chem. B* **2006**, *110*, 21667–21671.

[14] W. Q. Jiang, Z. Cao, R. Gu, X. Z. Ye, C. F. Jiang, X. L. Gong, *Smart Mater. Struct.* **2009**, *18*, 125013.

[15] W. S. Wang, L. Zhen, C. Y. Xu, J. Z. Chen, W. Z. Shao, *ACS Appl. Mater. Interfaces* **2009**, *1*, 780–788.

[16] I. Yamaguchi, M. Watanabe, T. Shinagawa, M. Chigane, M. Inaba, A. Tasaka, M. Izaki, *ACS Appl. Mater. Interfaces* **2009**, *1*, 1070–1075.

[17] F. Caruso, R. A. Caruso, H. Möhwald, *Science* **1998**, *282*, 1111–1114.

[18] S. W. Kim, M. Kim, W. Y. Lee, T. Hyeon, *J. Am. Chem. Soc.* **2002**, *124*, 7642–7643.

[19] H. Liang, H. Zhang, J. Hu, Y. Guo, L. Wan, C. Bai, *Angew. Chem. Int. Ed.* **2004**, *43*, 1540–1543.

[20] B. Z. Putlitz, K. Landfester, H. Fischer, M. Antonietti, *Adv. Mater.* **2001**, *13*, 500–503.

[21] J. Bao, Y. Liang, Z. Xu, L. Si, *Adv. Mater.* **2003**, *15*, 1832–1835.

[22] D. Zhang, L. Qi, J. Ma, H. Cheng, *Adv. Mater.* **2002**, *14*, 1499–1502.

[23] Q. Peng, Y. J. Dong, Y. D. Li, *Angew. Chem. Int. Ed.* **2003**, *42*, 3027–3030.

[24] X. W. Lou, C. L. Yuan, E. Rhoades, Q. Zhang, L. A. Archer, *Adv. Funct. Mater.* **2006**, *16*, 1679–1684.

[25] L. Y. Wang, J. Bao, L. Wang, F. Zhang, Y. D. Li, *Chem. Eur. J.* **2006**, *12*, 6341–6347.

[26] Y. D. Yin, R. M. Rioux, C. K. Erdonmez, S. Hughes, G. A. Somorjai, A. P. Alivisatos, *Science* **2004**, *304*, 711–714.

[27] H. G. Yang, H. C. Zeng, *J. Phys. Chem. B* **2004**, *108*, 3492–3495.

[28] Y. J. Xiong, B. Wiley, J. Y. Chen, Z. Y. Li, Y. D. Yin, Y. N. Xia, *Angew. Chem. Int. Ed.* **2005**, *44*, 7913–7917.

[29] Q. Liu, H. Liu, M. Han, J. Zhu, Y. Liang, Z. Xu, Y. Song, *Adv. Mater.* **2005**, *17*, 1995–1999.

[30] a) H. G. Zhang, Q. S. Zhu, Y. Zhang, Y. Wang, L. Zhao, B. Yu, *Adv. Funct. Mater.* **2007**, *17*, 2766–2771; b) J. H. Gao, B. Zhang, X. X. Zhang, B. Xu, *Angew. Chem. Int. Ed.* **2006**, *45*, 1220–1223.

[31] a) K. S. W. Sing, D. H. Everett, R. A. W. Haul, L. Moscou, R. A. Pierotti, J. Rouquerol, T. Siemieniewska, *Pure Appl. Chem.* **1985**, *57*, 603–619; b) Y. Kondo, H. Yoshikawa, K. Awaga, M. Murayama, T. Mori, K. Sunada, S. Bandow, S. Iijima, *Langmuir* **2008**, *24*, 547–550.

[32] J. Yu, X. Yu, *Environ. Sci. Technol.* **2008**, *42*, 4902–4907.

[33] J. G. Yu, G. H. Wang, B. Cheng, M. H. Zhou, *Appl. Catal. B* **2007**, *69*, 171–180.

[34] D. Lin-Vien, N. B. Colthup, W. G. Fateley, J. G. Grasselli, *The Handbook of IR and Raman Characteristic Frequencies of Organic Molecules*, Academic Press, New York, **1991**, pp. 45–59.

[35] G. Socrates, *Infrared Characteristic Group Frequencies*, Wiley, New York, **2001**, pp. 50–81.

[36] a) Y. Chang, J. J. Teo, H. C. Zeng, *Langmuir* **2005**, *21*, 1074–1079; b) B. Liu, H. C. Zeng, *Small* **2005**, *1*, 566–571.

[37] a) H. Cölfen, M. Antonietti, *Angew. Chem. Int. Ed.* **2005**, *44*, 5576–5591; b) H. Cölfen, S. Mann, *Angew. Chem. Int. Ed.* **2003**, *42*, 2350–2365; c) Y. Peng, A. W. Xu, B. Deng, M. Antonietti, H. Cölfen, *J. Phys. Chem. B* **2006**, *110*, 2988–2993.

[38] a) M. J. Seigfreid, K. S. Choi, *Angew. Chem. Int. Ed.* **2005**, *44*, 3218–3223; b) M. J. Seigfreid, K. S. Choi, *Adv. Mater.* **2004**, *16*, 1743–1746.

[39] F. Wang, X. G. Liu, *J. Am. Chem. Soc.* **2008**, *130*, 5642–5643.

[40] S. Mann, D. D. Archibald, J. M. Didymus, T. Douglas, B. R. Heywood, F. C. Meldrum, N. J. Reeves, *Science* **1993**, *261*, 1286–1292.

[41] Y. P. Li, J. H. Zhang, X. Zhang, Y. S. Luo, X. G. Ren, H. F. Zhao, X. J. Wang, L. D. Sun, C. H. Yan, *J. Phys. Chem. C* **2009**, *113*, 4413–4418.

[42] J. F. Suyver, J. Grimm, K. W. Krämer, H. U. Güdel, *J. Lumin.* **2005**, *114*, 53–59.

Received: November 18, 2009
Published Online: March 18, 2010

